Acta Crystallographica Section F
Structural Biology Communications
ISSN 2053-230X

Crystallization, room-temperature X-ray diffraction and preliminary analysis of Kaposi's sarcoma herpesvirus LANA bound to DNA

Jan Hellert,[a] Joern Krausze,[a] Thomas F. Schulz[b] and Thorsten Lührs[a,b]*

[a]Department of Structural Biology, Helmholtz Centre for Infection Research, Inhoffenstrasse 7, 38124 Braunschweig, Germany, and [b]Institute of Virology, Hannover Medical School, Carl-Neuberg-Strasse 1, 30625 Hannover, Germany

Correspondence e-mail: thorsten.luhrs@senostic.com

Received 20 May 2014
Accepted 3 September 2014

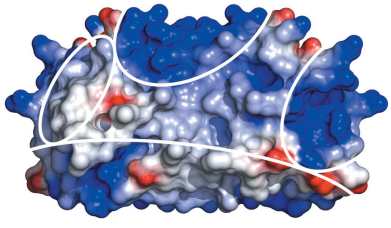

The latency-associated nuclear antigen (LANA) is the latent origin-binding protein and chromatin anchor of the Kaposi's sarcoma herpesvirus (KSHV/HHV-8) genome. Its C-terminal domain (CTD) binds sequence-specifically to the viral origin of replication, whereas the N-terminal domain links it to nucleosomes of cellular chromatin for long-term persistence in dividing host cells. Here, the crystallization and X-ray data acquisition of a mutant LANA CTD in complex with its wild-type target DNA LBS1 is described. This report describes the rational protein engineering for successful co-crystallization with DNA and X-ray diffraction data collection at room temperature on the high-brilliance third-generation synchrotron PETRA III at DESY, Germany.

1. Introduction

Kaposi's sarcoma herpesvirus (KSHV/HHV-8) is the causative agent of Kaposi's sarcoma, primary effusion lymphoma and the plasma-cell variant of multicentric Castleman's disease (Schulz, 2006). During latency, KSHV expresses only a small subset of its more than 90 open reading frames, one of which is the latency-associated nuclear antigen (ORF73/LANA; Kedes *et al.*, 1997; Rainbow *et al.*, 1997). The LANA protein binds sequence-specifically to its target sites within the minimal replicator in the viral terminal repeat region. LANA thus marks the viral genome for replication by the host machinery (Hu *et al.*, 2002; Lim *et al.*, 2002; Stedman *et al.*, 2004). It also interacts with mitotic chromosomes and thus mediates segregation of the viral genomes to daughter nuclei (Barbera *et al.*, 2006; Ballestas *et al.*, 1999). As a consequence of these attributes, LANA is strictly required for viral persistence throughout the course of a lifelong latent infection.

The high-affinity LANA-binding site (LBS1) within the GC-rich terminal repeat region has been described independently by three different groups (Cotter *et al.*, 2001; Ballestas & Kaye, 2001; Garber *et al.*, 2002). It harbours an 8 base pair (bp) palindrome, which, however, does not seem to be bound symmetrically by the homodimeric protein (Srinivasan *et al.*, 2004). A well resolved structure of the $LANA_2$–LBS1 complex would not only characterize a key macromolecular interaction in KSHV latency, but may also provide a valuable basis for the targeted rational development of a therapeutic antiviral LANA inhibitor.

2. Methods and results

2.1. Rational mutagenesis

We and others have previously solved the crystal structure of the C-terminal DNA-binding domain of KSHV LANA in the absence of DNA (Hellert *et al.*, 2013; Domsic *et al.*, 2013). We have also tried to obtain crystals of the wild-type LANA CTD (C-terminal domain) in complex with its target DNA. However, we observed that the addition of either specific or nonspecific DNA to different C-terminal LANA fragments immediately resulted in quantitative precipitation of both components. This effect was independent of the buffer, pH and ionic strength. It was also indicated previously that monodisperse LANA–DNA complexes are exceedingly difficult to obtain in the absence of appropriate high-molecular-weight blocking agents such as BSA (Han *et al.*, 2010).

Table 1
DNA constructs used in this study.

DNA fragment†	Sequence‡	Co-crystals with LANA(996–1149) mutant
LBS1(0–17)	5′-ctcccgcccgggcatggg-3′ 3′-gagggcgggcccgtaccc-5′	No
LBS1(0–17) palindrome '*A*'	5′-cCcATgcccgggcatggg-3′ 3′-gGgTAcgggcccgtaccc-5′	Thin plates
LBS1(0–17) palindrome '*B*'	5′-ctcccgcccgggcGGgAg-3′ 3′-gagggcgggcccgCCcTc-5′	No
LBS1[(−2)–22] A:T overhang	5′-Agcctcccgcccgggcatggggccgc-3′ 3′-cggagggcgggcccgtaccccggcgT-5′	No
LBS1(0–18)	5′-ctcccgcccgggcatgggg-3′ 3′-gagggcgggcccgtacccc-5′	No
LBS1(3–20)	5′-ccgcccgggcatggggcc-3′ 3′-ggcgggcccgtaccccgg-5′	No
LBS1(2–21)	5′-cccgcccgggcatggggccg-3′ 3′-gggcgggcccgtaccccggc-5′	Cubic crystals

† The numbering of the sequence corresponds to that of Srinivasan *et al.* (2004). ‡ The 8 bp palindrome is underlined. Bases differing from the original sequence are denoted by capital letters.

The dimeric KSHV LANA CTD is a highly basic domain which, in addition to its sequence-specific DNA-binding site, also contains other large positively charged patches (Fig. 1*a*). Moreover, the LANA CTD has the capacity to form higher-order oligomers by direct self-interaction through a hydrophobic patch. We reasoned that both these properties may contribute to its low solubility in the presence of any pure DNA *in vitro*.

Therefore, we inserted multiple point mutations into the wild-type sequence of the LANA CTD (Fig. 1*b*). Among those was a charge inversion of the 'lysine patch' by K1055E, K1138S, K1149D and K1141D. These mutations were inspired by the surface characteristics of Epstein–Barr virus EBNA1, which is a homologue of LANA (Bochkarev *et al.*, 1996). In addition, the lateral 'arginine patch' was attenuated by the mutations R1039Q and R1040Q. The single point mutation A1121E has previously been proven to disturb higher oligomerization efficiently and therefore was also included in the set (Hellert *et al.*, 2013). Finally, the two alanine substitutions K1109A and D1110A were introduced in order to increase the chances of favourable crystal contacts and to compensate for the loss of the native functional oligomerization interface.

Importantly, none of these mutations are located at the sequence-specific DNA-binding site, as defined by Kelley-Clarke and co-workers in their triple alanine-scanning mutagenesis screen (Kelley-Clarke *et al.*, 2007; Fig. 1*b*). Nevertheless, a LANA fragment of residues 996–1149 comprising this set of mutations was now highly soluble in the presence of specific DNA fragments under conditions of >0.3 *M* NaCl at pH 6.5.

2.2. Crystallization screening

Recombinant LANA protein was prepared by denaturing purification as described previously (Hellert *et al.*, 2013). A panel of DNA oligonucleotides was purchased from Sigma–Aldrich (purity: 'desalt'). Five DNA fragments comprised the wild-type high-affinity site LBS1, and two fragments were artificially perfect palindromes, the sequence of which was based on the wild-type imperfect palindrome (Table 1). Annealing was carried out at a concentration of 7.5 m*M* total ssDNA in 10 m*M* Tris–HCl pH 8.0 by passive cooling of a steel heating block from 95°C to room temperature overnight.

Commercial crystallization screens were employed in order to obtain the anticipated complex crystals by the vapour-diffusion method. A candidate crystal was considered to be positive when it met the following two criteria. Firstly, it should appear selectively with only one of the seven DNA constructs. Secondly, it should not appear when the above LANA CTD mutant was replaced by a different LANA CTD multiple point mutant of similar isoelectric point. While the protein alone robustly formed well diffracting $P6_122$ crystals under many ammonium sulfate conditions, two potential complex crystal forms were also obtained.

The first crystal form had a thin, plate morphology and appeared in the presence of the LBS1(0–17) palindrome '*A*' (Table 1). Crystals grew in condition Nos. 51, 55, 58 and 62 of the The Nucleix Suite (Qiagen) within three weeks at 22°C after adding 0.2 µl 0.75 m*M* LANA(996–1149) mutant, 0.57 m*M* dsDNA, 10 m*M* bis-tris pH 6.5, 0.5 *M* NaCl, 5 m*M* DTT to 0.2 µl reservoir solution in a sitting-drop setup. However, X-ray diffraction at −173°C was highly anisotropic with a maximum diffraction limit of 8 Å. Blurred spots were indicative of a high mosaicity. This crystal form was not improved any further.

A more promising, cubic crystal form was obtained in the presence of the wild-type LBS1(2–21) DNA fragment (Table 1). The largest initial crystals of 60 µm diameter grew in condition No. 27 of the The Nucleix Suite within one week at 22°C after adding 0.2 µl 1.20 m*M* LANA(996–1149) mutant, 0.72 m*M* dsDNA, 10 m*M* bis-tris pH 6.5, 0.85 *M* NaCl, 5 m*M* DTT to 0.2 µl reservoir solution consisting of 50 m*M* sodium cacodylate pH 6.5, 30% PEG 8000, 0.2 *M* ammonium acetate, 10 m*M* magnesium acetate in a sitting-drop setup. Crystal

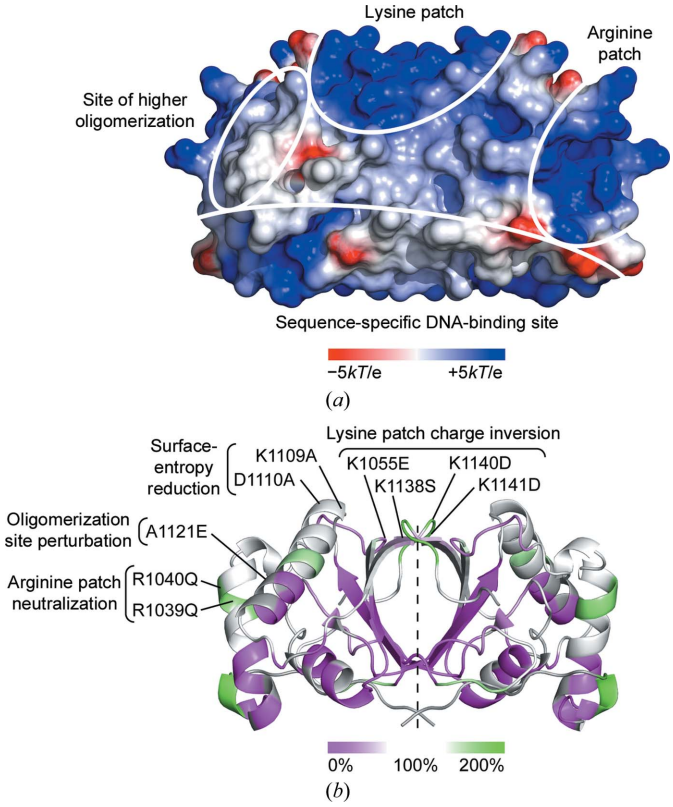

Figure 1
Structure of the KSHV LANA CTD dimer. (*a*) Van der Waals surface representation colour-coding the electrostatic potential. Characteristic features are highlighted. (*b*) Cartoon representation colour-coding triple alanine-scanning mutagenesis data regarding sequence-specific DNA binding in electrophoretic mobility shift assays (Kelley-Clarke *et al.*, 2007). Magenta, mutants are impaired in DNA binding; green, mutants display apparently stronger DNA binding; grey, not tested. Point mutations implemented in our LANA CTD constructs are indicated on the left monomer. The twofold symmetry axis is shown as a dashed line.

size was further increased by optimization of the conditions and subtle shortening of the protein fragment at both the N-terminus and the C-terminus. Crystals of up to 240 µm in size could be obtained within 5 d at 24°C after adding 0.9 µl 1.60 m*M* LANA(1008–1146) mutant, 0.96 m*M* dsDNA, 10 m*M* bis-tris pH 6.5, 0.9 *M* NaCl, 5 m*M* DTT to 0.9 µl reservoir solution consisting of 50 m*M* MES pH 6.6, 27% PEG 4000, 0.3 *M* ammonium acetate in a hanging-drop setup (Fig. 2).

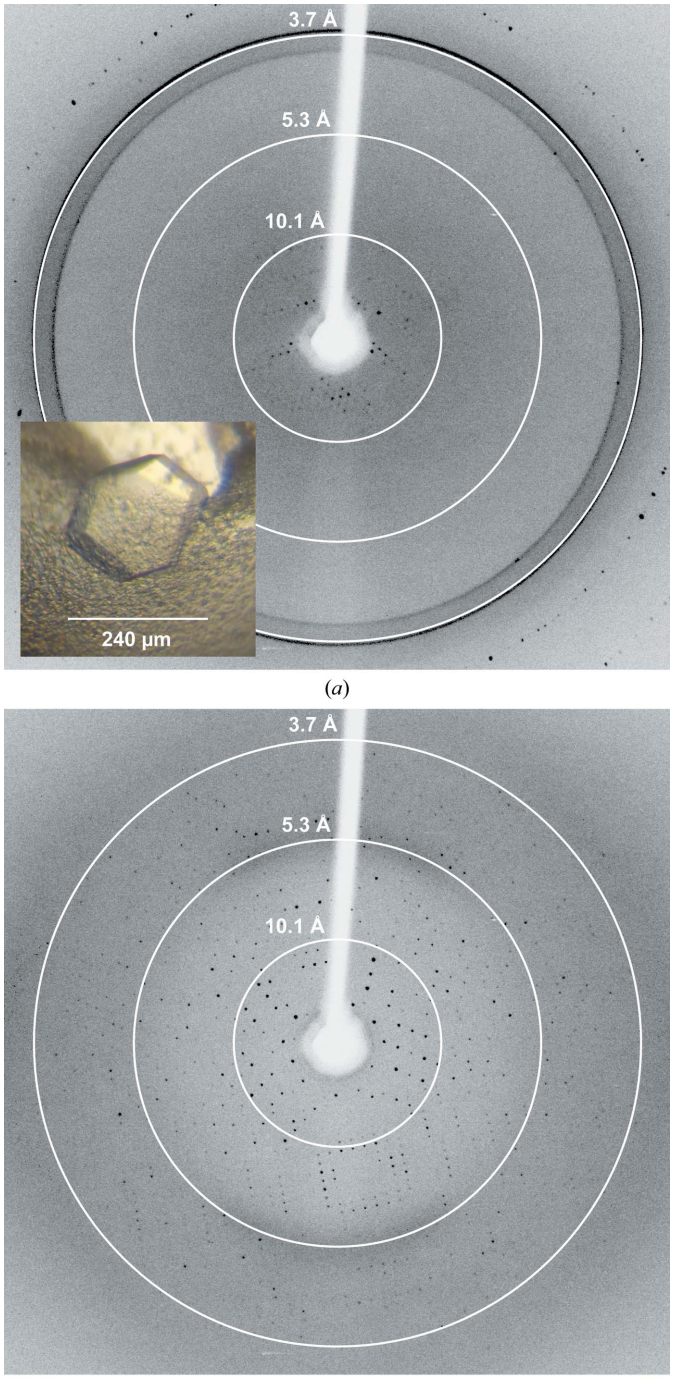

Figure 2
Representative X-ray diffraction images of optimized $I2_13$ crystals recorded on our home X-ray setup. (*a*) A cryocooled crystal without cryoprotection was measured at −173°C. Inset: typical morphology of the $I2_13$ crystals. (*b*) An identical crystal was measured at 20°C.

2.3. Data collection and processing

In order to cryoprotect the cubic crystals prior to cryocooling in liquid nitrogen, we initially tested glycerol or low-molecular-weight polyethylene glycols combined with different NaCl concentrations within the optimized reservoir-solution formulation. However, the crystals were found to be highly sensitive. Contact with glycerol or changes in the NaCl concentration by more than 0.1 *M* induced a slow dissolution of the crystals. In line with these observations, even macroscopically well preserved crystals did not diffract after short immersion in the cryoprotective solutions. In contrast, without any cryoprotection, the directly cryocooled crystals diffracted to about 10 Å resolution (Fig. 2*a*). It was subsequently discovered that this weak diffraction capacity could be markedly improved by measuring at room temperature. Using MicroRT capillaries (MiTeGen) to prevent dehydration, crystals diffracted beyond 3.7 Å resolution on our home X-ray setup (Fig. 2*b*). Owing to the sensitivity of the crystals towards osmotic shock and their limited number, we decided not to screen for a suitable cryoprotectant formulation any further.

A complete data set was collected from a single crystal on beamline P11 of the PETRA III synchrotron, DESY, Germany at T = 20°C. Images were recorded on a PILATUS 6M detector with an oscillation of 0.2° and an exposure time of 200 ms per frame. A pinhole of 50 µm was chosen for the incident beam while transmission was set to 40%, resulting in a nominal photon flux of 8×10^{10} photons s^{-1}. Further increasing the transmission did not improve the diffraction limit on

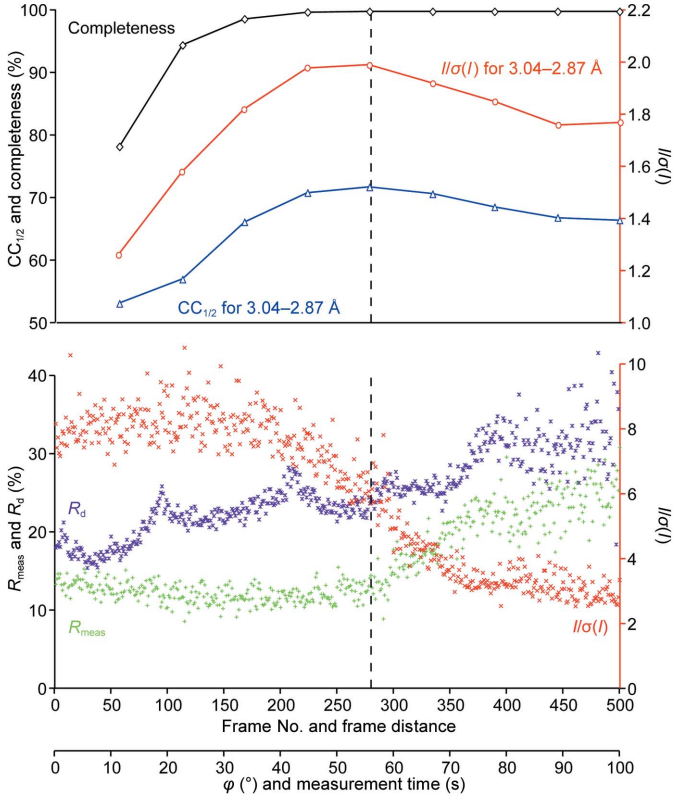

Figure 3
Data-set statistics plotted against the frame number. The top panel shows overall completeness as well as the cumulative $I/\sigma(I)$ and $CC_{1/2}$ for the highest resolution bin after processing the data set up to the respective frame number (Karplus & Diederichs, 2012). Data were generated using *XDS* (Kabsch, 2010). The lower panel shows total $I/\sigma(I)$, R_d and R_{meas} for individual frames or frame distances (Diederichs, 2006; Diederichs & Karplus, 1997). Data were generated with *XDSSTAT*. The dashed line indicates where the final data set was cut.

Table 2
Data collection and processing.

Values in parentheses are for the outer shell.

X-ray source	Beamline P11, PETRA III, DESY, Germany
Nominal photon flux (photons s^{-1})	8×10^{10}
Wavelength (Å)	1.00
Temperature (°C)	20
Detector	PILATUS 6M
Crystal-to-detector distance (mm)	397.08
Rotation range per image (°)	0.2
Total rotation range (°)	56
Exposure time per image (s)	0.2
Space group	$I2_13$
a, b, c (Å)	177.84, 177.84, 177.84
α, β, γ (°)	90, 90, 90
Mosaicity (°)	0.058
Resolution range (Å)	47.53–2.87 (3.04–2.87)
Total No. of reflections	137568 (21789)
No. of unique reflections	21605 (3452)
Completeness (%)	99.9 (99.7)
Multiplicity	6.4 (6.3)
$\langle I/\sigma(I)\rangle$	15.65 (1.99)
R_{meas} (%)	8.9 (93.3)
Overall B factor from Wilson plot ($Å^2$)	79.3

the first couple of images for identical crystals. Still, diffraction quality decreased in the course of the measurement, owing to the accumulation of radiation damage (see R_d and R_{meas} in Fig. 3).

The data set was processed using *XDS* (Kabsch, 2010). In order to determine the optimal frame number for the final data set, the cumulative $I/\sigma(I)$ and $CC_{1/2}$ of the highest resolution shell were chosen as quality indicators (Fig. 3, upper panel). It was found that both values reached a peak when no more than the first 280 frames were included in the set. Beyond this mark, a sudden increase of R_{meas} of the individual frames was observed, whereas the total $I/\sigma(I)$ of the individual frames started dropping around frame number 200 (Fig. 3, lower panel). The final data set comprising 280 frames covers a total angular range of 56° and has a high-resolution limit of 2.87 Å, with a cumulative $I/\sigma(I)$ in the highest resolution shell of 1.99 (Table 2).

2.4. Preliminary data analysis

Molecular replacement (MR) with *Phaser-MR* was used to break the space-group ambiguity and to obtain initial phases (McCoy *et al.*, 2007). As a search model, we used chain *A* of our previously determined decameric ring structure of the LANA CTD (PDB entry 2ypy; Hellert *et al.*, 2013). Although a single dimer of the search model could be placed in both space groups $I2_13$ and $I23$, the log-likelihood gain and translation function *Z*-score were better for the former (LLG = 1359.2, *Z*-score = 23.3 for $I2_13$ and LLG = 148.9, *Z*-score = 8.2 for $I23$). Additionally, only in $I2_13$ was electron density for the bound dsDNA fragment visible. This density was accounted for by placing an idealized 20 bp double-stranded DNA helix, which was subsequently adapted. Considering the total molecular weight of the $LANA_2$–dsDNA complex, the solvent content of the crystal has an exceptionally high value of 79.2% (Matthews, 1968). This high porosity is likely to be responsible for the sensitivity of the crystals towards cryoprotectants and cryocooling. Adding cryoprotectants to the crystals and the corresponding osmotic pressure could have resulted in a massive outflow of water. Cryocooling without cryoprotection, on the other hand, can result in an expansion of the water contained within the crystal, which is more critical for crystals with high solvent content. Both effects, however, cause mechanical stress that could damage the crystal. The high solvent content also prompted us to evaluate the diffraction quality of a single mounted crystal during passive dehydration in a MiTeGen MicroRT capillary over time. However, no significant improvement was observed at any time point. A more complete picture of the behaviour of the crystals at variant solvent contents may be obtained in the future by using a humidity-control device (Kiefersauer *et al.*, 2000; Russi *et al.*, 2011). The structure is currently being refined.

3. Conclusion

The C-terminal domain of KSHV LANA binds viral DNA in a sequence-specific manner. Rational protein engineering was successfully employed in order to overcome the low solubility of the pure specific complex in solution. Subsequent crystallization screening yielded cubic crystals belonging to space group $I2_13$ that were highly sensitive towards cryocooling. However, the high internal symmetry of these crystals allowed a redundant data set to be recorded from a single crystal at room temperature on a highly brilliant light source. For lower-symmetry space groups, however, a lower beam transmission may be chosen. Moreover, for large crystals a helical data-collection strategy should be considered whenever possible (Zeldin *et al.*, 2013). However, at the time of our measurements this option had not yet been implemented at the beamline. The crystal structure of KSHV LANA bound to its target DNA will shed yet more light on the molecular details of the lifelong latent persistence of a human pathogenic gammaherpesvirus.

Parts of this research were carried out at the PETRA III light source at DESY, a member of the Helmholtz Association (HGF). We would like to thank Anja Burkhardt for assistance in using beamline P11. This work was supported by the DFG Collaborative Research Centre SFB900 'Chronic Infections: Microbial Persistence and its Control' to TFS, by HGF grant VH-GS-202 to the HZI GradSchool and by the DFG Emmy Noether Young Investigator Grant LU1471/3-1 to TL.

References

Ballestas, M. E., Chatis, P. A. & Kaye, K. M. (1999). *Science*, **284**, 641–644.
Ballestas, M. E. & Kaye, K. M. (2001). *J. Virol.* **75**, 3250–3258.
Barbera, A. J., Chodaparambil, J. V., Kelley-Clarke, B., Joukov, V., Walter, J. C., Luger, K. & Kaye, K. M. (2006). *Science*, **311**, 856–861.
Bochkarev, A., Barwell, J. A., Pfuetzner, R. A., Bochkareva, E., Frappier, L. & Edwards, A. M. (1996). *Cell*, **84**, 791–800.
Cotter, M. A., Subramanian, C. & Robertson, E. S. (2001). *Virology*, **291**, 241–259.
Diederichs, K. (2006). *Acta Cryst.* D**62**, 96–101.
Diederichs, K. & Karplus, P. A. (1997). *Nature Struct. Biol.* **4**, 269–275.
Domsic, J. F., Chen, H.-S., Lu, F., Marmorstein, R. & Lieberman, P. M. (2013). *PLoS Pathog.* **9**, e1003672.
Garber, A. C., Hu, J. & Renne, R. (2002). *J. Biol. Chem.* **277**, 27401–27411.
Han, S. J., Hu, J., Pierce, B., Weng, Z. & Renne, R. (2010). *J. Gen. Virol.* **91**, 2203–2215.
Hellert, J., Weidner-Glunde, M., Krausze, J., Richter, U., Adler, H., Fedorov, R., Pietrek, M., Rückert, J., Ritter, C., Schulz, T. F. & Lührs, T. (2013). *PLoS Pathog.* **9**, e1003640.
Hu, J., Garber, A. C. & Renne, R. (2002). *J. Virol.* **76**, 11677–11687.
Kabsch, W. (2010). *Acta Cryst.* D**66**, 125–132.
Karplus, P. A. & Diederichs, K. (2012). *Science*, **336**, 1030–1033.
Kedes, D. H., Lagunoff, M., Renne, R. & Ganem, D. (1997). *J. Clin. Invest.* **100**, 2606–2610.
Kelley-Clarke, B., Ballestas, M. E., Srinivasan, V., Barbera, A. J., Komatsu, T., Harris, T. A., Kazanjian, M. & Kaye, K. M. (2007). *J. Virol.* **81**, 4348–4356.
Kiefersauer, R., Than, M. E., Dobbek, H., Gremer, L., Melero, M., Strobl, S., Dias, J. M., Soulimane, T. & Huber, R. (2000). *J. Appl. Cryst.* **33**, 1223–1230.
Lim, C., Sohn, H., Lee, D., Gwack, Y. & Choe, J. (2002). *J. Virol.* **76**, 10320–10331.
Matthews, B. W. (1968). *J. Mol. Biol.* **33**, 491–497.

McCoy, A. J., Grosse-Kunstleve, R. W., Adams, P. D., Winn, M. D., Storoni, L. C. & Read, R. J. (2007). *J. Appl. Cryst.* **40**, 658–674.
Rainbow, L., Platt, G. M., Simpson, G. R., Sarid, R., Gao, S. J., Stoiber, H., Herrington, C. S., Moore, P. S. & Schulz, T. F. (1997). *J. Virol.* **71**, 5915–5921.
Russi, S., Juers, D. H., Sanchez-Weatherby, J., Pellegrini, E., Mossou, E., Forsyth, V. T., Huet, J., Gobbo, A., Felisaz, F., Moya, R., McSweeney, S. M., Cusack, S., Cipriani, F. & Bowler, M. W. (2011). *J. Struct. Biol.* **175**, 236–243.
Schulz, T. F. (2006). *J. Pathol.* **208**, 187–198.
Srinivasan, V., Komatsu, T., Ballestas, M. E. & Kaye, K. M. (2004). *J. Virol.* **78**, 14033–14038.
Stedman, W., Deng, Z., Lu, F. & Lieberman, P. M. (2004). *J. Virol.* **78**, 12566–12575.
Zeldin, O. B., Gerstel, M. & Garman, E. F. (2013). *J. Synchrotron Rad.* **20**, 49–57.